Information content of point radiance measurements in turbid media: implications for interstitial optical property quantification

Lee C. L. Chin, William M. Whelan, and I. Alex Vitkin

Motivated by a recent report by Dickey *et al.* [Phys. Med. Biol. **46,** 2359 (2001)], who demonstrated optical property retrieval by using relative radiance measurements at a single position, we investigate the uniqueness of relative radiance measurements for quantifying the optical properties of turbid media by studying the solutions of the diffusion and $P3$ approximations of the Boltzmann transfer equation for a point source. Using the $P3$ approximation, we investigate the potential of radiance measurements for optical property recovery by examining the optical property response surface for point radiance information. We further derive first-order similarity relations for relative point radiance measurements and use these expressions to examine analytically the effects of noise on optical property retrieval over a wide range of optical properties typical of biological tissue. Finally, optimal experimental configurations are studied and explicit conditions for uniqueness derived that suggest potential strategies for improving optical property recovery. It is expected that point radiance measurements will prove valuable for both on-line treatment planning of minimally invasive laser therapies and optical characterization of tissues.

OCIS codes: 170.6510, 170.7050, 170.3660, 290.1990, 290.4210.

1. Introduction

The determination of tissue optical properties has long been important in the biophotonics community for quantitative determination of functional parameters (e.g., chromophore concentration) and planning for treatment of laser-based therapies. Typically, one determines optical properties by fitting the diffusion theory for light transport in tissue to relative fluence measurements performed at known source–detector locations. The absorption and scattering properties are inherently separable by use of spatially resolved relative steady-state measurements because the fluence measured one mean free path (MFP) from the source is primarily a function of the scattering properties, while the fluence several MFPs from the source is due to both scattering and absorption. Using surface reflectance geometry, one can sample a range of source–detector locations to provide unique optical property determination in a noninvasive manner. Interstitially, however, measurements one MFP from the source are impractical owing to invasiveness and inaccurate positioning. With such limitations, a range of different optical interaction parameters can result in the same spatial light distribution. The mathematical expressions that relate such equivalent parameters are known as similarity relations.[1] To overcome the limitations of optical similarity, interstitial characterization of tissue optical properties has typically required absolute fluence measurements,[2,3] which can be difficult to obtain accurately.

Recently the development of directional sensors has allowed for an alternative to traditional fluence characterization and monitoring of laser therapies.[4,5] Using relative radiance measurements at a single distance and the $P3$ approximation as a model for fitting, Dickey *et al.*[6] demonstrated the ability to characterize the optical properties of liquid optical phantoms. Their research indicated that radiance information obtained at a single spatial position may allow for more localized recovery of optical properties than can spatially resolved fluence methods, without the requirement of absolute calibration. However, their research was limited to a single optical property

L. C. L. Chin (chinl@uhnres.utoronto.ca), W. M. Whelan, and I. A. Vitkin are with the Department of Medical Biophysics, University of Toronto and Ontario Cancer Institute, Toronto M5G 2M9, Canada; W. M. Whelan is also with the Department of Biophysics and Bioengineering. W. M. Whelan is also with the Department of Physics, Ryerson University, Toronto M5B 2K3, Canada.

Received 10 June 2005; revised 17 September 2005; accepted 20 September 2005.

0003-6935/06/092101-14$15.00/0

pair and set of experimental parameters, and a more comprehensive study is necessary to demonstrate the full potential of this technique. In particular, the range of optical properties over which radiance measurements can accurately recover optical properties and the optimal experimental parameters necessary to do so have yet to be studied. Furthermore, it was unclear whether the $P3$ approximation is a necessary model for inversion or whether the commonly used diffusion theory is sufficient for fitting.

In this paper we examine the uniqueness of optical property recovery from relative point radiance measurements over a broad range of properties typical of biological tissue with and without noise. To do so we expand on the fluence work of Wyman *et al.*[1] and derive similarity expressions for point relative radiance information. We further examine the optimal sensor positions, angular sampling intervals, and angular ranges for radiance-based optical property characterization. Finally, we present practical strategies for improving optical property retrieval. Such analysis guides the experimental design under which unique optical property determination is achievable.

The paper is organized as follows: In Sections 2 and 3 we present the analytical $P3$ radiance expression and examine the regimes whereby the $P3$ model converges to the diffusion approximation for radiance. In Section 4 we review briefly the experimental limitations typically encountered in interstitial steady-state fluence measurements and comment on how they lead to nonunique optical property recovery. The potential of radiance measurements is demonstrated by use of Monte Carlo (MC) simulations. In Section 5 we compare the performance of both the diffusion and $P3$ approximations for modeling point radiance measurements against MC simulations over a selected range of sensor positions and albedos. In Section 6 the chi-square terrain of relative point radiance data is studied. In Section 7 similarity relations are derived, and in Section 8 a new technique presented for studying the uncertainty of point radiance measurements for recovering optical properties in the presence of noise. Using this technique, we examine the uncertainty of point radiance optical property determination over a wide range of optical properties typical of biological tissue. In Section 9 we establish optimal experimental conditions for radiance-based retrieval of optical properties, and in Section 10 we suggest practical experimental strategies for improved optical property recovery. Finally, we conclude with a brief discussion of the implications of our results.

2. *P*3 Approximation to the Boltzmann Transport Equation

In this study we utilize the P_N approximations to the Boltzmann transport equation for the radiance, L, that results from a point source emitting light in an infinite, homogeneous, turbid medium. These solutions are obtained by expansion of the Boltzmann transport equation to Nth order for the radiance, phase function, and source as a series of Legendre polynomials and by solving the resultant set of coupled equations for the relevant boundary conditions. Particularly close to the source, radiance measurements are sensitive to the exact form of the phase function, which is generally unknown *a priori.* Although it is unable to completely describe the measured phase functions of all biological tissues, the Henyey–Greenstein phase function[7] was recently applied in forward models to extract local chromophore concentrations in reflectance geometry at close source–detector separations in rat tumor[8] and determine optical properties by using point radiance measurements in *ex vivo* human prostate.[6] In the research reported here, unless stated otherwise, the Henyey–Greenstein phase function was used to model the light scattering in tissue. Owing to the asymmetry of the Legendre polynomials, odd-order solutions are better suited for modeling asymmetries in the forward and backward radiance and, therefore, tend to be more accurate than their preceding even-order expansions in describing the light distribution near boundaries and in low-albedo media.[9] Truncation of the Boltzmann transport equation to first order leads to the well-known diffusion approximation, whereas a third-order expansion results in the $P3$ approximation. The diffusion approximation has commonly been applied as an inversion algorithm despite its restrictions at locations proximal to the source and for low scattering media. However, extension to the $P3$ approximation has been shown to provide accurate quantification of optical properties at distances less than one MFP and for albedos as low as 0.59.[10] Hull and Foster[10] previously demonstrated the validity of the $P3$ approximation by comparison with MC simulations over a wide range of optical properties that are typical of biological tissues.[10] The resultant expression for radiance is

$$L(r,\theta) = S_o \sum_{l=0}^{3} \frac{2l+1}{4\pi} \left[C' h_l(-v^-) Q_l(-v^- r) + D' h_l(-v^+) Q_l(-v^+ r) \right] P_l(\theta). \quad (1)$$

Here r is the radial source–detector separation and θ is the detection angle relative to the radial normal vector. S_o is the source power. v^+ and v^- are eigenvalues that result from the third-order expansion of the transport equation and are similar to the effective attenuation coefficient, μ_{eff}, and the reduced transport coefficient, μ_t', in the diffusion approximation, respectively. P_l are Legendre polynomials of order $l = (0, 1, 2, 3)$, while Q_l are given by the recurrence relation $Q_l(x) = Q_{l-2}(x) - (2l - 1/x)Q_{l-1}(x)$, with $Q_o(x) = \exp(x)/x$ and $Q_1(x) = (1 - 1/x)\exp(x)/x$. h_l are functions of either v^+ or v^- and the medium's optical properties and are

$$h_o(v^\pm) = 1, \qquad h_1(v^\pm) = \frac{\mu_a}{v^\pm},$$

$$h_2(v^\pm) = \left[-\frac{1}{2} + \frac{3\mu_a \mu_t^{(1)}}{2v^{\pm 2}} \right],$$

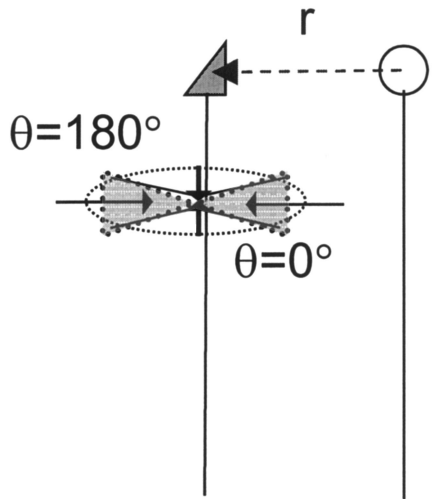

Fig. 1. Geometry for point radiance measurements.

$$h_3(v^{\pm}) = \left[-\frac{9\mu_a\mu_t^{(1)}}{14\mu_t^{(3)}v^{\pm}} + \frac{3v^{\pm}}{14\mu_t^{(3)}} \right], \tag{2}$$

where $\mu_t^{(l)} \equiv \mu_a + \mu_s'^{(l)}$, $\mu_l^{(0)} = \mu_a$, $\mu_s'^{(l)} \equiv \mu_s(1 - g^l)$, and $v^{\pm}$ is either v^+ or v^-. In the diffusion approximation, $\mu_s'^{(l)} \equiv \mu_s' = \mu_s'(1 - g)$, which is the commonly known reduced scattering coefficient. However, in the $P3$ approximation the second- and third-order expansions of the phase function result in two higher-order values of μ_s'. To facilitate comparison with the commonly utilized diffusion theory μ_s', we employ the relations derived by Hull and Foster[10]:

$$\mu_s(1 - g_2) = 1.85\ \mu_s', \quad \mu_s(1 - g_3) = 2.6\ \mu_s'. \tag{3}$$

They demonstrated by comparison with MC simulations the validity of these relations over the range $0.7 \le g \le 0.99$.

Finally, C' and D' are derived from the boundary conditions: continuity of radiance, conservation of power, and finite radiance as $r \to \infty$, and are given by[10]

$$C' = -\frac{(v^-)^2}{2\pi} \frac{v^{-3}\left[3\mu_a\mu_t^{(1)} - v^{+2}\right]}{\left[6\mu_a^2\mu_t^{(1)}\left(v^{-2} - v^{+2}\right)\right]},$$

$$D' = -\frac{(v^-)^2}{2\pi} \frac{v^{+3}\left[3\mu_a\mu_t^{(1)} - v^{-2}\right]}{\left[6\mu_a^2\mu_t^{(1)}\left(v^{+2} - v^{-2}\right)\right]}. \tag{4}$$

Note that, in Eq. (1), P_l describe the angular shape of each mode and the bracketed terms provide their relative contributions to the total radiance. Figure 1 presents a schematic of the relevant experimental geometry whereby radiance information is collected by means of a right-angle probe at a distance r from an isotropic source. At r, a radiance profile can be obtained by rotation of the sensor from $\theta = 0°$ (the collecting side of the sensor faces the source) to $\theta = 180°$ (the sensor faces away from the source). The numerical aperture of a radiance sensor can be explicitly accounted for by integration of Eq. (1) over a known acceptance angle. However, Dickey *et al.* previously showed experimentally that θ is well approximated by the center angle of collected radiance.[6]

3. Convergence of *P*1 and *P*3 Approximations

Here we examine how the $P3$ solution converges to the diffusion approximation for radiance. Hull and Foster[10] and Boas[11] previously demonstrated that, when reduced albedo $a = \mu_s'/\mu_s' + \mu_a$ is in the range $a \ge 0.8, v^- \cong \mu_{\text{eff}}$. Furthermore, as $D'h_l(-v^+)Q_l(-v^+r)$ is a term that contributes significantly only at source–detector separations of less an approximately two transport MFPs, one can assume that at several MFPs from the source this term can be neglected.[11]

Using the diffusion relation $\mu_{\text{eff}}^2 = 3\mu_a u_t^{(1)}$ and noting that $v^{+2} \gg 3\mu_a\mu_t^{(1)} \gg v^{-2}$, we find that

$$C' \to \frac{1}{2\mu_a}\mu_{\text{eff}}^{-2}, \quad h_1(v^-) \to -\frac{\mu_a}{\mu_{\text{eff}}},$$

$$h_2(v^-) \to \left[-\frac{1}{2} + \frac{\mu_{\text{eff}}^2}{2\mu_{\text{eff}}^2} \right] = 0,$$

$$h_3(v^-) \to \left[-\frac{3\mu_{\text{eff}}^2}{14\mu_t^{(3)}\mu_{\text{eff}}} + \frac{3\mu_{\text{eff}}}{14\mu_t^{(3)}} \right] = 0. \tag{5}$$

Under conditions that satisfy the diffusion approximation, the second and third moments containing the $h_l(v^-)$ coefficients defined by Eqs. (2) go to zero. Furthermore, when Eq. (1) is expanded to the first two moments and relations (5) are used instead of Eqs. (2) and (4), we arrive at the familiar diffusion theory solution for radiance[12]:

$$L(\boldsymbol{r},\ \theta) = \frac{P_o}{4\pi}\frac{1}{4\pi rD}\left[1 + 3\left(D/r + \sqrt{\mu_a D}\right)\cos\theta\right] \times \exp(-\mu_{\text{eff}}\, r), \tag{6}$$

with $D = 1/3(\mu_s' + \mu_a)$. When the higher-order terms are added, slight deviations from Eq. (6) begin to arise to account for lower albedos and close source positions. Hence the diffusion approximation is valid only where there is a minimal contribution from the second- and third-order modes, which is the case for turbid media with high albedos and spatial positions far from sources or boundaries. Although it is limited as a forward model for optical property retrieval, Eq. (6) provides a simplified, analytical expression that may be used to study explicitly the uniqueness of relative point radiance measurements for recovering optical properties (as we show below in Sections 7 and 8).

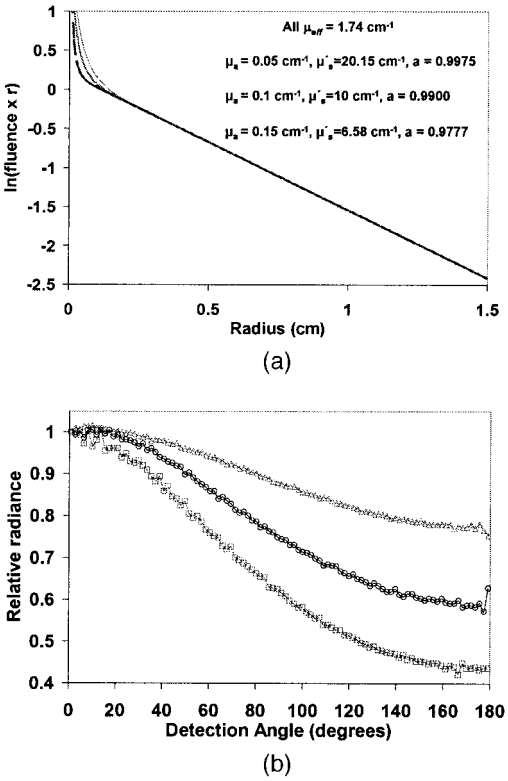

Fig. 2. (a) Monte Carlo simulations of fluence distribution normalized to $r = 0.5$ cm for three combinations of μ_a and μ_s' and the same μ_{eff}. Beyond ~0.2 cm the three profiles are virtually indistinguishable. (b) Monte Carlo simulations of the radiance distribution normalized to $\theta = 0.9°$ at $r = 1$ cm for the same optical property combinations as for (a). The three curves are well separated despite the equivalent fluence distributions.

4. Information Content of Relative Steady-State Measurements

In the case of relative fluence measurements, a fully sampled spatial distribution at one MFP and several MFPs from the source is required for unique determination of the scattering and absorption properties of turbid media. This is demonstrated in Fig. 2a, which shows that MC simulations adapted from a previous platform[15,16] were used to generate fluence distributions with three different reduced albedos and the same μ_{eff} of 1.74 cm^{-1}, as a function of radial distance r, from the source. The resultant relative fluence distributions are normalized to $r = 0.5$ cm for the three optical property sets. At distances less than ~0.2 cm, the curves are clearly separated and appear unique. However, experimentally, interstitial measurements one MFP from the source are generally impractical owing to invasiveness and inaccurate positioning. Under such limitations, a range of different optical interaction parameters can result in the same spatial light distribution. Notice that beyond ~0.2 cm the fluence distributions converge, becoming virtually identical. This interplay between scattering and absorption, which can lead to identical fluence profiles generated with different optical properties, has been called optical similarity by Wyman *et al.*[1] and underscores the difficulty in characterizing optical properties with relative steady-state fluence measurements. To overcome the limitations of optical similarity, optical property retrieval using fluence measurements typically requires an experimentally determined calibration factor, C_V, to convert photovoltage readings to absolute fluence. It is difficult to obtain factor C_V accurately,[13,14] making unique determination of optical properties impossible if the calibration factor is not known. Figure 2(b), however, shows the potential of using relative radiance information for optical property recovery. Again, we used MC simulations to obtain relative radiance profiles at 1 cm from the source by using the same three sets of optical property that generated the fluence profiles in Fig 2(a). Because of the finite angular bin size ($\Delta\theta = 1.8°$) used in the MC simulations, the radiance profiles are normalized to $\theta = 0.9°$ and not to 0°. The three curves are well separated despite the equivalence in the effective attenuation coefficient. Although Fig. 2 illustrates the increased information content of point radiance measurements relative to spatial fluence profiles, the key to optical property characterization is whether, analogous to the fluence approach, optical similarity relations exist for relative radiance measurements with a single sensor. If they do, the unique determination of optical coefficients based on radiance data may be impossible.

5. Accuracy of Diffusion and *P*3 Approximations: Comparison with Monte Carlo Simulations

In Section 4 the potential of relative radiance measurements was demonstrated through MC simulations. Although they are accurate, MC simulations are generally ill suited for data fitting because of their long computational times. Therefore in this section we briefly explore the diffusion and *P*3 approximations as potential forward models for optical property determination by using relative radiance measurements.

Figure 3 shows the resultant diffusion and *P*3 radiance profiles compared with MC results for input parameters of $\mu_s' = 10$ cm^{-1} and $\mu_a = 0.01$, 1.75 cm^{-1} at $r = 0.5$, 1.3 cm. The conditions were chosen to demonstrate clearly where the diffusion and *P*3 converge and to compare the performance of the *P*3 approximation under conditions when the diffusion approximation breaks down (close to the sources and for low albedos). In Figs. 3(a) and 3(b), μ_s' is 1000 times larger than μ_a, satisfying a well-known condition for diffusion theory. Despite the high albedo, Fig. 1(a) shows that at a close source-detector separation of ~5 transport paths from the source ($r = 0.5$ cm) the diffusion approximation greatly deviates from MC results, whereas the *P*3 approximation shows excellent agreement. As indicated in Section 3, the diffusion and *P*3 solutions converge at larger source–detector separations ($r = 1.3$ cm), both demonstrating good agreement with MC results [Fig. 1(b)]. By contrast, in Figs. 3(c) and 3(d), μ_s' is only 5.7 times greater than μ_a. As may be

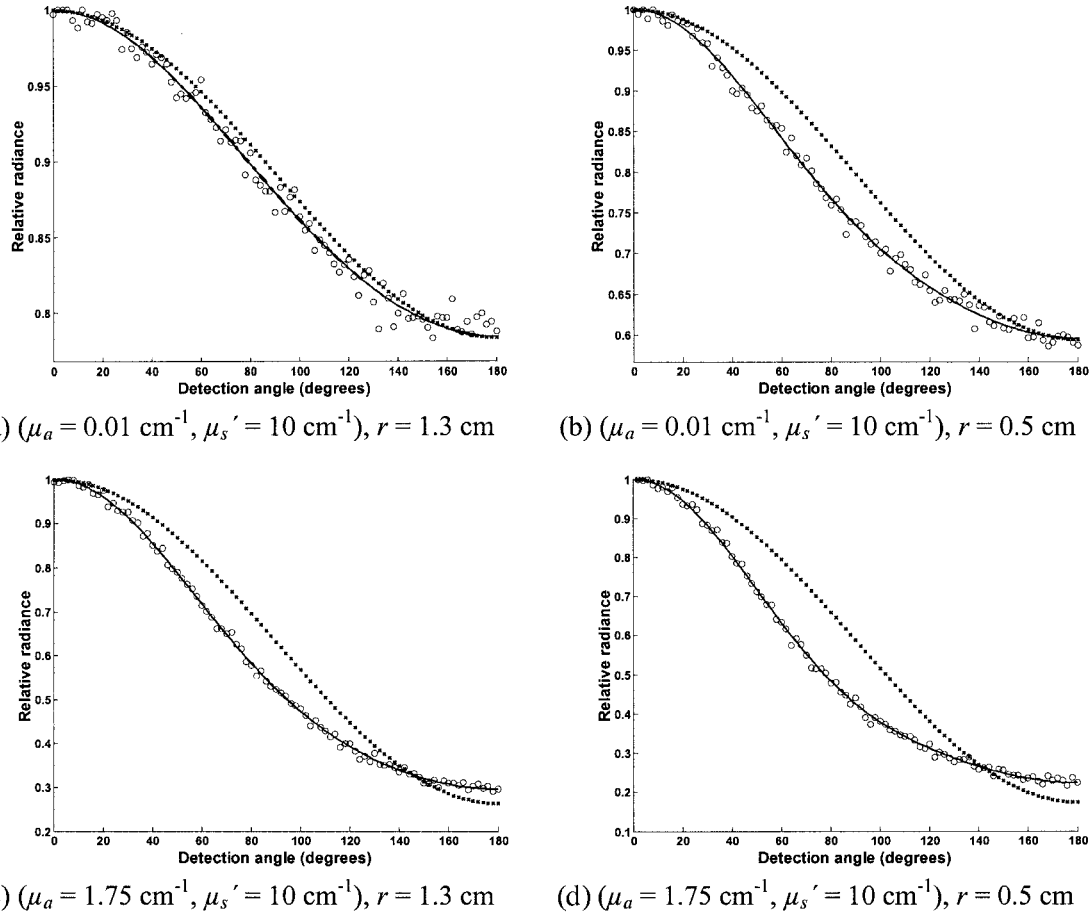

Fig. 3. Comparison of Monte Carlo (circles) generated relative radiance versus the diffusion (dotted curves) and $P3$ (solid curves) forward models for optical property sets of ($\mu_a = 0.01$ cm^{-1}, $\mu_s' = 10$ cm^{-1}) and ($\mu_a = 1.75$ cm^{-1}, $\mu_s' = 10$ cm^{-1}) at sensor positions of $r = 0.5$, 1.3 cm.

expected from the previous case, far from the source at $r = 1.3$ cm, one might expect the light field to be well described by the diffusion approximation. Yet Fig. 1(d) shows that, even 15 transport paths from the source, in the case of low albedos the diffusion approximation again provides a poor description of the radiance. By contrast, the $P3$ approximation provides excellent agreement in all conditions presented, even for the low-albedo case at $r = 0.5$ cm where diffusion theory performs most poorly. The cases above satisfy a wide range of typical experimental conditions. However, even in the $P3$ approximation, early truncation of the phase function results in inaccuracies of the model at positions too close to the source. This breakdown typically occurs at low albedos but is virtually nonexistent beyond several MFPs from the source. Therefore we restricted our analysis to a starting sensor position greater than or equal to 5 mm. Furthermore, at this distance and for optical properties typical of tissue in the near-infrared window, radiance measurements are much less sensitive to the exact form of the phase function.[17] Unless otherwise noted, all forward calculations for the remainder of this paper are performed with the P3 approximation.

6. Chi-Square Space Examination of the Uniqueness of Relative Point Radiance Measurements

To determine optical properties by using radiance information, one must find a set of absorption and reduced scattering coefficients that, when they are input into the $P3$ forward model, generate a radiance profile that minimizes the chi-square difference, χ^2, relative to the experimentally measured radiance profile in the medium being characterized. The χ^2 function is described mathematically as

$$\chi^2(\mu_a, \mu_s') = \sum_{i=1_1}^{N(\theta)} \left(\frac{\{L[(r,\ \theta^i)_{\exp} - L_{P3}(r,\ \theta^i,\ \mu_a,\ \mu_s')_{P3}]\}^2}{\delta_{\exp}{}^{i2}} \right). \quad (7)$$

$L_{\exp}$ is the experimental radiance at position r and measured at the ith detection angle, θ^i. In this study, detection angles ranging from 0° to 180° with 2° angular resolution were used. Parameters r and θ^i are assumed known during fitting. L_{P3} is the relative radiance obtained with the analytical $P3$ approximation from the vector of parameters u =

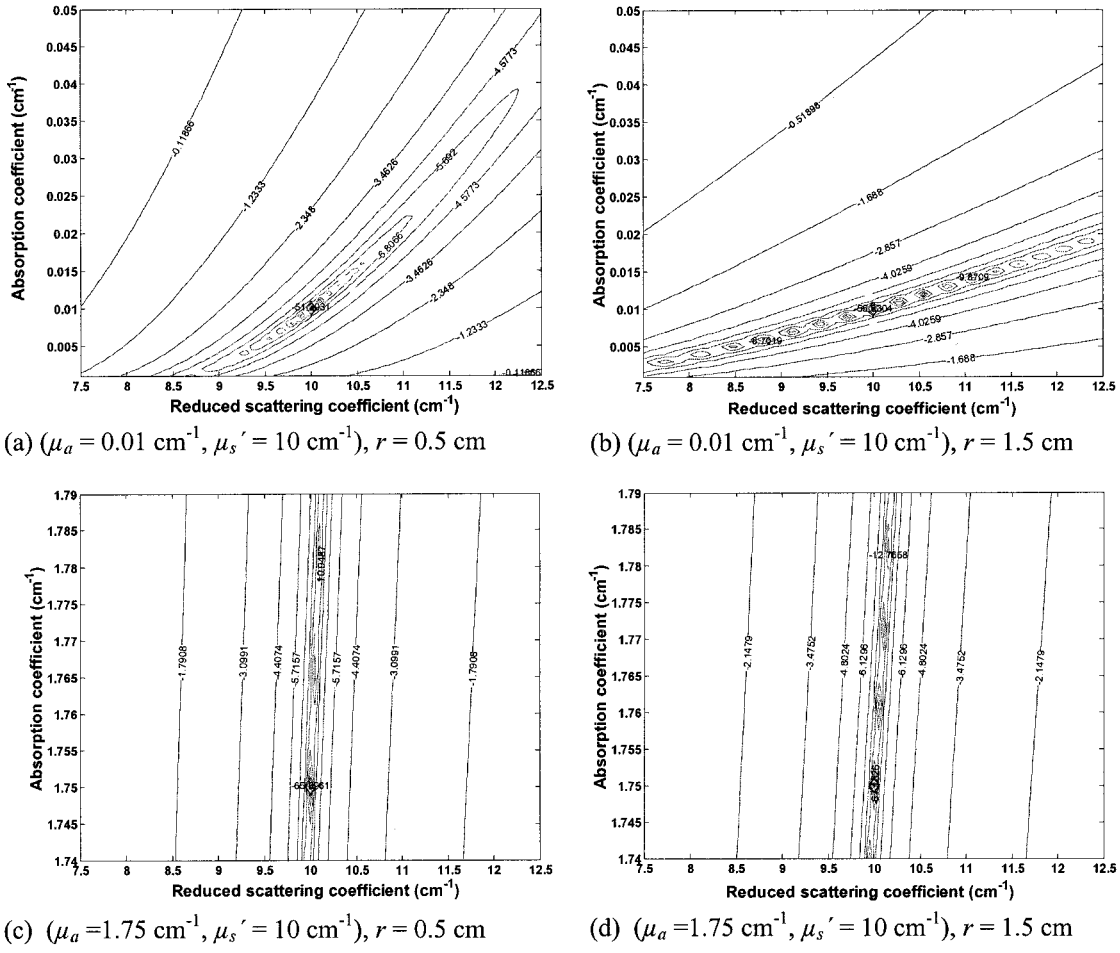

Fig. 4. Chi-square surfaces generated with the $P3$ forward model for optical property sets of (μ_a = 0.01 cm^{-1}, μ_s' = 10 cm^{-1}) and (μ_a = 1.75 cm^{-1}, μ_s' = 10 cm^{-1}) at sensor positions of r = 0.5, 1.5 cm.

[r, θ^i, μ_a, μ_s'], while $\delta_{\exp}{}^i$ is the standard deviation of the radiance at each detection angle (1 for noiseless conditions).

For a radiance profile $L_{\exp}$ to be unique for a given (μ_a, μ_s') pair, a global minimum must arise when Eq. (7) is calculated over all possible (μ_a, μ_s') combinations. Nonuniqueness can arise when multiple minima are associated with the same radiance profile or when experimental noise is larger than the χ^2 difference between the absolute minimum and its surrounding valleys. To determine whether a global minimum exists for point radiance measurements, we generate contour plots of χ^2 values as a function of μ_a and μ_s'. The terrain of such plots, also known as χ^2 space or the response surface, can provide indications of whether convergence to a unique solution is likely to occur during fitting.

Here we present four contour plots, shown in Fig. 4, whereby $L_{\exp}$ is simulated by use of the $P3$ approximation for two sets of nominally true (μ_a, μ_s') pairs: (μ_a = 0.01 cm^{-1}, μ_s' = 10 cm^{-1}) and (μ_a = 1.75 cm^{-1}, μ_s' = 10 cm^{-1}) and two sensor positions, r = 0.5, 1.5 cm. We chose these parameters with which to examine the difference in χ^2 terrain between two distinct albedos and sensor positions. The χ^2 differences are very small, with each contour line typically representing a value from 10^{-1} to 10^{-70}, and, as such, are presented on a log scale for clarity.

Examining Fig. 4, we find that the response surface is analogous to a river bed extending across the entire examined χ^2 space and located at the bottom of a rapidly descending valley. Examining the region of absolute minima in Fig. 4, we see that, in all cases, the χ^2 space reveals concentrically decreasing valleys surrounding an absolute minimum located at a (μ_a, μ_s') pair corresponding to the true properties. Small islands of minima scattered within the lowest χ^2 valley are also observed. The presence of such islands can lead to nonunique solution sets in the presence of noise and to cross talk in optical properties during fitting.

Examining the χ^2 topography for the two different sensor positions, we observe that, for both property sets, a higher density of minima exists about the absolute minimum for the 1.5 compared with the 0.5 cm value. This is particularly evident for the low-absorption case. Similarly, comparison of the χ^2 topography for the two property sets for the same sensor position sets demonstrates a higher density of surrounding minima for (μ_a = 0.01 cm^{-1}, μ_s'

$= 10\ \mathrm{cm}^{-1}$) than for ($\mu_a = 1.75\ \mathrm{cm}^{-1}$, $\mu_s' = 10\ \mathrm{cm}^{-1}$). The χ^2 plots appear to indicate that, for the optical properties studied, radiance data obtained from high μ_a media and close sensor positions are more likely to converge to a true solution during fitting than low μ_a media and far sensor positions. In Sections 8 and 9 below, we present a more comprehensive analysis over a wider range of property sets and sensor positions.

The existence of a global minimum located at the true properties suggests that under noiseless conditions optical properties can indeed be determined by use of a single radiance sensor. However, although only one global minimum exists, the absolute difference between the surrounding χ^2 valleys is small and, in the presence of increasing noise or random errors, results in an expanded number of possible solution sets. In Section 7 we derive explicit analytical expressions that provide a first-order estimation of optical property pairs that produce the lowest χ^2 values surrounding the global minimum. These optical property sets result in χ^2 values that lie close to the global minimum and, as such, are likely solutions during fitting. Therefore, by studying their χ^2 values relative to a predefined noise threshold we can examine the effects of noise on optical property determination without the requirement of sampling over all of χ^2 space.

7. First-Order Similarity Relations for Relative Point Radiance at a Single Position

The $P3$ generated χ^2 plots in Fig. 4 demonstrate that, over the typical range of expected optical properties of biological tissues, an absolute minimum exists. However, in this section we show that first-order similarity solution sets exist for relative point radiance measurements and that, experimentally, the inability to detect the second- and third-order modes may lead to nonuniqueness for radiance characterization of tissues.

Starting with the diffusion approximation expression for radiance, Eq. (6) contains the P_o term typically required for calibrating photovoltage readings to absolute radiance. To remove this term we normalize Eq. (6) to any radiance detection angle and arrive at

$$L_{\mathrm{rel}}(\mathbf{r},\ \theta) = C\left[1 + 3\left(D/r + \sqrt{\mu_a D}\right)\cos\theta\right]. \qquad (8)$$

Here C is a known constant determined by the normalization angle. When $\theta = 90°$, $C = 1$ and it is clear that, in the case of linear anisotropy, the radiance is a straight line in $\cos\theta$ with the intercept always known *a priori* and the slope a function of the optical properties and sensor position. Expanding the slope explicitly as a function of μ_a and μ_s' gives

$$K = \frac{1}{(\mu_s' + \mu_a)}\left\{1/r + \left[3\mu_a(\mu_s' + \mu_a)\right]^{1/2}\right\}. \qquad (9)$$

K is a constant that describes the radiance distribution at r calculated by use of the true properties and is independent of the angle by which the radiance distribution is normalized. A unique solution would require that only one μ_s', μ_a pair satisfy K. However, rearranging Eq. (9) yields a quadratic equation in μ_a:

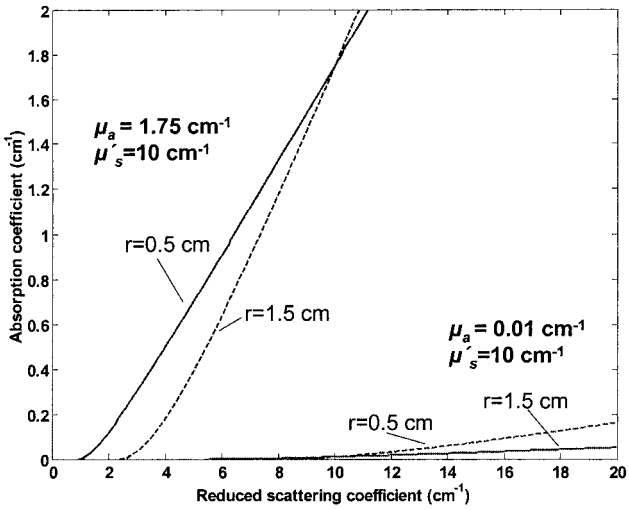

Fig. 5. Optical property pairs that generate the same relative radiance distribution for two optical property sets at sensor positions of 0.5 and 1.5 cm.

$$A\mu_a^2 + B\mu_a + C = 0,$$

$$A = K^2 - 3,$$

$$B = 2K^2\mu_s' - \frac{2K}{r} - 3\mu_s',$$

$$C = (K\mu_s')^2 - \frac{2K\mu_s'}{r} + \frac{1}{r^2}. \qquad (10)$$

Equation (10) states that at a given sensor position r and for any μ_s', there exists a μ_a that results in the same K. It is interesting that below a minimum μ_s' value, (μ_a, μ_s') pairs determined from Eq. (10) do not satisfy Eq. (9). The reason for this is that these optical properties lie outside the validity of the diffusion regime. We can determine the minimum reduced scattering coefficient, $\mu_{s,\min}'$, by setting $\mu_a = 0$ in Eq. (10) and solving for μ_s'. Below $\mu_{s,\min}'$, μ_a decreases until it reaches a minimum at 0 and then increases again above $\mu_{s,\min}'$, resulting in two possible μ_s' values' being associated with identical μ_a to generate the same radiance profile. Therefore the breakdown of Eq. (10) below $\mu_{s,\min}'$ may also be explained physically because no two μ_s' can be associated with the same μ_a.

Figure 5 plots the resulting similar solution sets for radiance curves generated by use of the same nominal true properties examined in Fig. 2 ($\mu_s' = 10\ \mathrm{cm}^{-1}$, $\mu_a = 0.01,\ 1.75\ \mathrm{cm}^{-1}$ at $r = 0.5,\ 1.5$ cm). Examining Fig. 5, we see that μ_a increases almost linearly as a function of increasing μ_s' to maintain the same radiance shape. Because of the effective atten-

uation coefficient, $\mu_{\text{eff}} = [3\mu_a(\mu_s' + \mu_a)]^{1/2}$, similar solution sets for relative radiance measurements have unique μ_{eff}. This result is in contrast to first-order similarity relations for fluence where μ_a must decrease with increasing μ_s' to maintain the same overall attenuation. Comparing the $P3$ generated χ^2 plots of Fig. 4 with those of Fig. 5, we notice that the similar optical property pairs of Fig. 4 are equivalent to the locations of the deepest χ^2 valleys of Fig. 4.

However, unlike the χ^2 plots generated by use of the $P3$ approximation, a global minimum does not occur with the $P1$ approximation, indicating that uniqueness emerges because of the presence of the second- and third-order modes. Therefore the ability to experimentally detect the second- and third-order modes will determine whether optical properties can be uniquely recovered. Such limitations are dependent on the noise level of the measurements. In Section 8, we describe a simple noise model relevant to typical radiance measurements performed in our lab and present a method that uses the first-order similarity relations derived in this section to investigate the expected fractional uncertainty in recovered optical properties owing to noise.

8. Uncertainty Analysis of Point Radiance Optical Property Recovery

A. Noise Model

Given ideal experimental conditions, the uncertainty in the measured radiance signal at each detection angle is determined by random voltage fluctuations from the detector. However, in most practical situations the dominant uncertainty in the amplitude is due to random errors in detection angle. To investigate the effects of noise on point radiance optical property recovery, we simulate two different noise models: random rotational errors and root-mean-square root-mean-square noise in the photodiode, and utilize the $P3$ approximation as a forward model to simulate experimental measurements.

In our experiments a radiance probe is rotated mechanically on an automated stage. The rotational stage has a 2° resolution and an estimated worst-case 0.5° uncertainty for each detection angle θ^i. This uncertainty is simulated directly by randomly distributing errors at each detection angle θ^i from $-0.5°$ to $+0.5°$. The new noisy detection angles are substituted into the $P3$ forward model to generate noisy radiance measurements, $L_{r,\text{noise}}$.

The root-mean-square noise is simulated by use of a worst-case manufacturer-quoted 0.1% fluctuation in the photodiode (Thorlabs) and was estimated from a range of photovoltages measured experimentally for various radiance detection angles at sensor positions of 0.5 and 1.5 cm (from the source) in Intralipid phantoms with optical properties ranging from $\mu_s' = 10\ \text{cm}^{-1}$ and $\mu_a = 0.01\text{–}5\ \text{cm}^{-1}$. This noise is assumed to follow a normal distribution and is added to $L_{r,\text{noise}}$.

B. Analysis of Uncertainty in Optical Property Recovery Owing To Noise

The first-order similar-solution sets obtained from Eq. (10) can be utilized to estimate the uncertainty in recovered optical properties that is due to experimental noise. Recall that, in χ^2 space, these optical properties lie close to the global minimum and therefore become potential solutions in the presence of noise. As an example, Fig. 5 plots χ^2 values as functions of μ_s' and μ_a where L_{exp} in Eq. (7) is calculated from the $P3$ approximation with the true properties of $\mu_{a,\text{true}} = 1.75\ \text{cm}^{-1}$ and $\mu_{s,\text{true}}' = 10\ \text{cm}^{-1}$ while L_{P3} is calculated with the corresponding similar optical property sets determined by Eq. (10). A sensor position of $r = 1.0$ cm is used in the calculations.

Figure 5 is essentially a cross section of the deepest valley in χ^2 space. Also shown is the χ^2 threshold determined by addition of the experimentally estimated noise described in Subsection 8.A to L_{exp}. The optical properties associated with χ^2 values below the noise threshold are potential solutions during fitting. The span of these potential solutions is determined from the minimum and maximum μ_s' or μ_a x-axis values where the noise threshold intersects the χ^2 curve [shown in Figs. 6a and 6(b)]. As a further demonstration, Fig. 7 plots the corresponding relative radiance curves generated by use of the true properties with and without noise and the corresponding minimum ($\mu_a = 1.6\ \text{cm}^{-1}$, $\mu_s' = 8.93\ \text{cm}^{-1}$) and maximum ($\mu_a = 2.07\ \text{cm}^{-1}$, $\mu_s' = 11.42\ \text{cm}^{-1}$) optical property sets, which are virtually indistinguishable from each other.

The fractional difference, ε_{MAX} (or ε_{MIN}), between $\mu_{s,\text{true}}'$ and the maximum $\mu_{s,\text{MAX}}'$ (or minimum $\mu_{s,\text{MIN}}'$) reduced scattering coefficient is given by

$$\varepsilon_{\text{MAX}} = \frac{|\mu_{s,\text{true}}' - \mu_{s,\text{MAX}}'|}{\mu_{s,\text{true}}'}. \tag{11}$$

ε_{MAX} and ε_{MIN} are then averaged to provide a measure of the uncertainty, ε_{avg}, in recovered optical properties by use of a single radiance sensor. A similar equation is used to calculate ε_{avg} for $\mu_{a,\text{true}}$. The method described provides an analytical technique with which to reasonably estimate the effects of random noise and is independent of the fitting algorithm used for inversion, thereby allowing a direct assessment of information content to be made. Here we analyze the the intrinsic information content of radiance measurements only when the exact experimental parameters are assumed known. It should be noted that, when one is investigating the effects of systematic errors, direct fitting algorithms such as singular-value decomposition or Levenberg–Marquardt inversion must be utilized.

C. Optical Property Dependence

Figures 8(a) and 8(b) show contour plots of ε_{avg} calculated by the method described in Subsection 8.B for μ_a and μ_s', respectively, with μ_s' ranging from 5 to 15 cm^{-1} and μ_a spanning 0.01 to 5 cm^{-1}. The re-

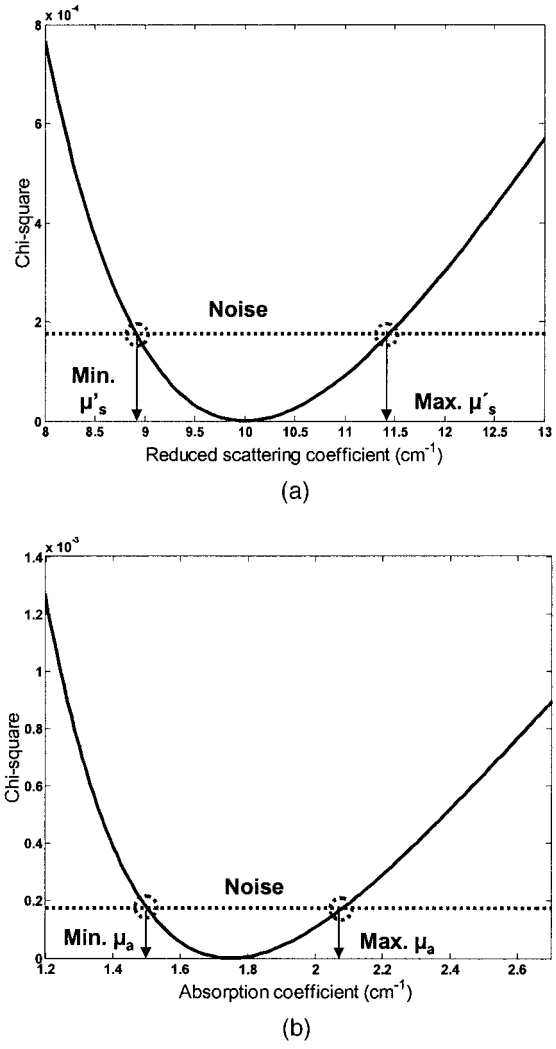

Fig. 6. χ^2 difference between $P3$ radiance distributions calculated by use of the true properties of ($\mu_a = 1.75\ \text{cm}^{-1}$, $\mu_s' = 10\ \text{cm}^{-1}$) and similar optical property pairs generated with Eq. (10) as a function of (a) μ_s' and (b) μ_a at 1 cm. Dotted lines, the χ^2 difference between radiance generated by the use of the true properties with and without noise. The intersection point of the χ^2 distribution with the noise threshold provides an estimation of the minimum ($\mu_a = 1.6\ \text{cm}^{-1}$, $\mu_s' = 8.03\ \text{cm}^{-1}$) and the maximum ($\mu_a = 2.07\ \text{cm}^{-1}$, $\mu_s' = 11.42\ \text{cm}^{-1}$) deviations in optical properties owing to noise.

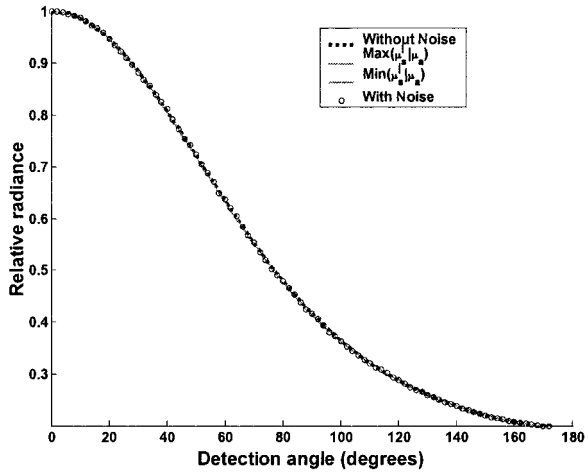

Fig. 7. Relative radiance distribution for optical properties of $\mu_a = 1.75\ \text{cm}^{-1}$, $\mu_s' = 10\ \text{cm}^{-1}$, and $r = 1.0$ cm (dashed black curve). Circles, the same radiance distribution with added noise. Also plotted are the radiance distributions for the minimum ($\mu_a = 1.6\ \text{cm}^{-1}$, $\mu_s' = 8.03\ \text{cm}^{-1}$) and the maximum ($\mu_a = 2.07\ \text{cm}^{-1}$, $\mu_s' = 11.42\ \text{cm}^{-1}$) deviations in optical properties that are due to noise (solid green curve). Within the noise level, the curves are virtually identical.

sults are presented for a radiance sensor located at $r = 1$ cm and θ ranging from 0° to 180° with 2° resolution. Figure 8 demonstrates that radiance determination of μ_a is more sensitive to noise than μ_s', with the uncertainty generally 1.5–2 times greater for μ_a than for μ_s'. Examining the overall topography for both μ_a and μ_s' reveals two general trends.

First, for a given fixed μ_s', the uncertainty increases as μ_a increases. This trend is likely due to an increase in sensitivity from rotational error as the radiance field becomes increasingly anisotropic (e.g., the radiance field changes more rapidly as a function of detection angle) at higher μ_a. This conclusion is supported by our observation that, if no rotational error is present, only a minor increase in fractional uncertainty is observed with increasing μ_a (data not shown).

Similarly, for a given fixed μ_a, the uncertainty also increases as μ_s' increases. This trend is likely due to the emergence of an expanded number of optically similar solution sets as the diffusion regime is approached at higher μ_s'. The increase in uncertainty is mirrored in χ^2 space, where, for a given fixed μ_a, the absolute minima become progressively shallower relative to their surrounding terrain as μ_s' increases (data not shown). Such shallow minima are particularly sensitive to noise because, for the same noise threshold, a larger set of potential similar solution sets exists than for χ^2 terrain with a steeply descending global minimum.

The results indicate that, in general, for media with $\sim\mu_s' \leq 11\ \text{cm}^{-1}$ and $\mu_a \leq 2\ \text{cm}^{-1}$, optical property recovery with relative radiance measurements is optimal, while determination of optical properties in media with properties outside this range is recovered with greater uncertainty. Still, overall the contour plots indicate that optical properties are expected to be recovered with maximum uncertainties no greater than 25% (under the noise and experimental conditions quoted). However, in practice, systematic errors such as in positioning may arise that increase the overall error.

9. Optimizing Experimental Design and Strategies

In Section 8 we demonstrated that, owing to small differences in the surrounding χ^2 valleys about the true minimum, radiance measurements are affected by experimental noise. This investigation was performed at fixed sensor position, angular resolution, and angular sampling range. In this section, using the noise analysis described in Subsection 8.B, we

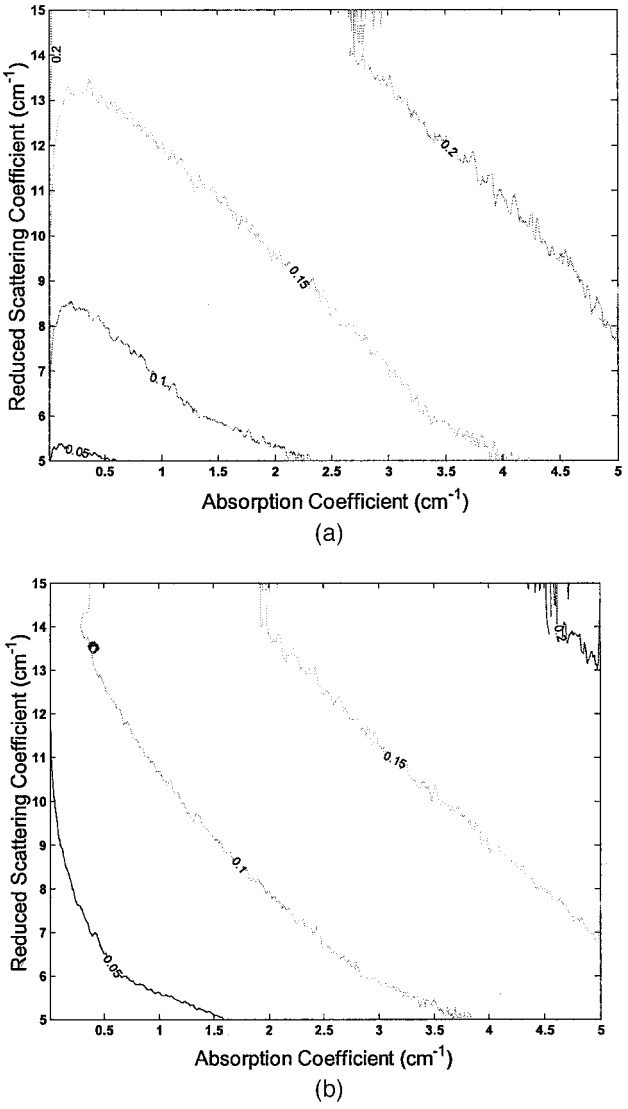

Fig. 8. Contour plots of maximum uncertainty in recovered (a) μ_a and (b) μ_s' owing to the presence of experimental noise at a sensor position of 1 cm.

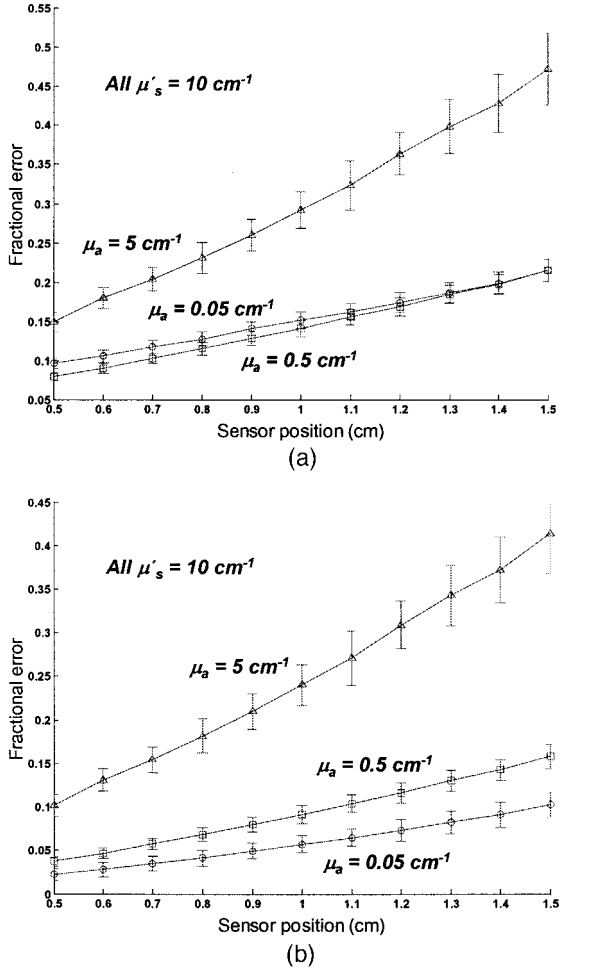

Fig. 9. Fractional uncertainty owing to noise in recovered (a) μ_a and (b) μ_s' for three optical property sets as a function of increasing source–sensor separation.

investigate the geometries and angular sampling criteria that optimize the information content of point radiance measurements. In all cases, error bars are the standard deviation of ε_{avg} calculated from 100 randomly generated noisy radiance distributions.

A. Sensor Position

Figures 9(a) and 9(b) plot ε_{avg} for μ_a and μ_s', respectively, as a function of sensor position r for nominal true optical properties of $\mu_s' = 10\ \text{cm}^{-1}$ and $\mu_a = 0.05,\ 0.5,\ 5\ \text{cm}^{-1}$. These optical properties were chosen to span a large attenuation and albedo range for typical tissues. The plots demonstrate that the fractional uncertainty increases as a function of increasing sensor position with uncertainties increasing by approximately 2–4 times for both μ_a and μ_s' as r is moved from 0.5 to 1.5 cm. This demonstrates that radiance measurements close to the source provide more-accurate recovery of optical properties than do measurements far from the source. The likely explanation is that farther from the source, we approach the diffusion approximation regime in which differences between the forward and backward radiance decrease. This overall flattening of the radiance profile results in a loss of distinctiveness and sensitivity. The results suggest that, if possible, radiance sensors should be positioned no greater than ~1 cm apart for accurate optical property characterization. Although close source–detector positions are preferable for accurate quantification, as stated above, measurements adjacent to the source begin to exhibit inaccuracies in the $P3$ model and for typical optical properties in the near infrared are limited to a minimum measurement position of ~0.5 cm.

B. Angular Sampling Interval and Maximum Sampling Angle

Figures 10(a) and 10(b) plot ε_{avg} for μ_a and μ_s', respectively, as a function of angular sampling interval $\Delta\theta$ for nominal optical properties of $\mu_s' = 10\ \text{cm}^{-1}$ and $\mu_a = 0.05,\ 0.5,\ 5\ \text{cm}^{-1}$ and a fixed sensor position of $r = 1$ cm. In all cases, measurements span 0° to

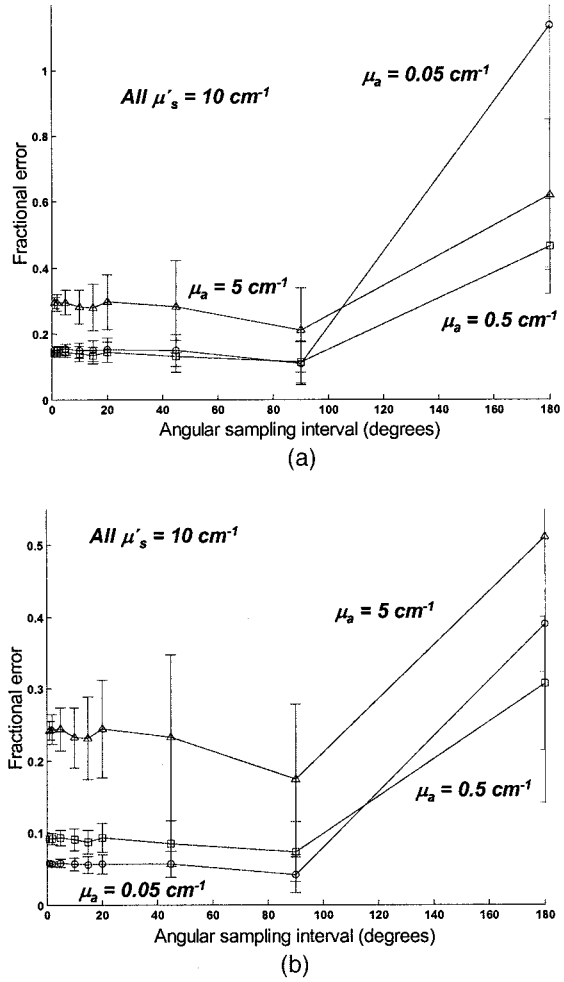

Fig. 10. Fractional uncertainty owing to noise in recovered (a) μ_a and (b) μ_s' as a function of angular sampling interval for three optical property sets and a sensor position of 1 cm. All radiance data span an angular range of 0°–180°.

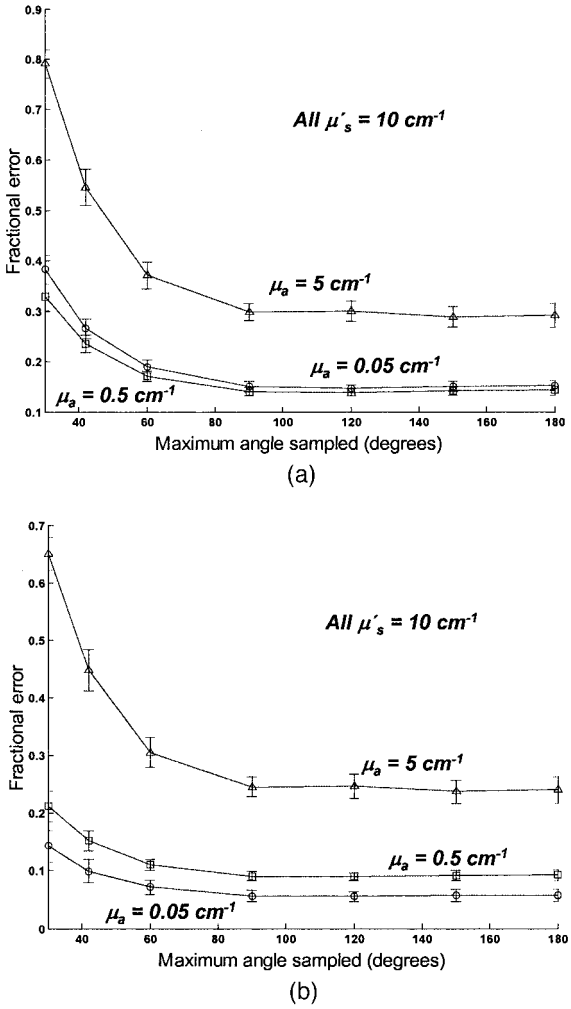

Fig. 11. Fractional uncertainty owing to noise in recovered (a) μ_a and (b) μ_s' as a function of maximum angle sampled for three optical property sets and a sensor position of 1 cm.

180° with a 90° sampling interval containing three measurements (at 0°, 90°, and 180°) and a 1° sampling interval that has 181 measurements. Interestingly, the angular sampling interval appears to have a minimal effect on the overall uncertainty in recovered optical properties, with a difference of only ~1% between $\Delta\theta = 1°$ and $\Delta\theta = 45°$, and although it is well within the error bars of the data, only a slightly larger difference of ~8% at $\Delta\theta = 90°$. However, at an angular sampling interval of 180°, a large jump in uncertainty occurs, as one might expect with only two measurements.

The angular sampling range ($\theta = 0°$ to the maximum sampling angle, θ_{MAX}), however, plays a more crucial role for accurate point radiance characterization of optical properties. Figure 11 plots the relative error as a function of θ_{MAX}, using the same optical properties and sensor position as above. In all cases, angular sampling interval $\Delta\theta$ was adjusted such that the radiance curve was composed of 90 equally spaced measurement from $\theta = 0°$ to θ_{MAX}. The results demonstrate that both μ_s' and μ_a can be optimally characterized, provided that a minimum 90° scan is performed. Beyond 90°, no significant improvement in optical property characterization is observed. This indicates that optimal point radiance characterization requires measurements with angular sampling intervals of at least 90° and with the total number of measurements relatively unimportant.

Figures 12(a) and 12(b) are contour plots that demonstrate the dependence of ε_{avg} on both $\Delta\theta$ and θ_{MAX} for a fixed optical property set of $\mu_a = 0.5\ cm^{-1}$ and $\mu_s' = 10\ cm^{-1}$. The plots verify the general conclusions of Figs. 10 and 11 and show that for the optical properties under consideration a value of $\Delta\theta$ of less than ~90° combined with a value of θ_{MAX} no less than 90° is required for both μ_s' and μ_a are to be recovered with better than ~15% accuracy.

10. Uniqueness Conditions for Relative Radiance in the Diffusion Approximation

Although it is convenient to utilize single sensors to characterize tissue optical properties, it is reasonable to assume that, adding additional relative radiance

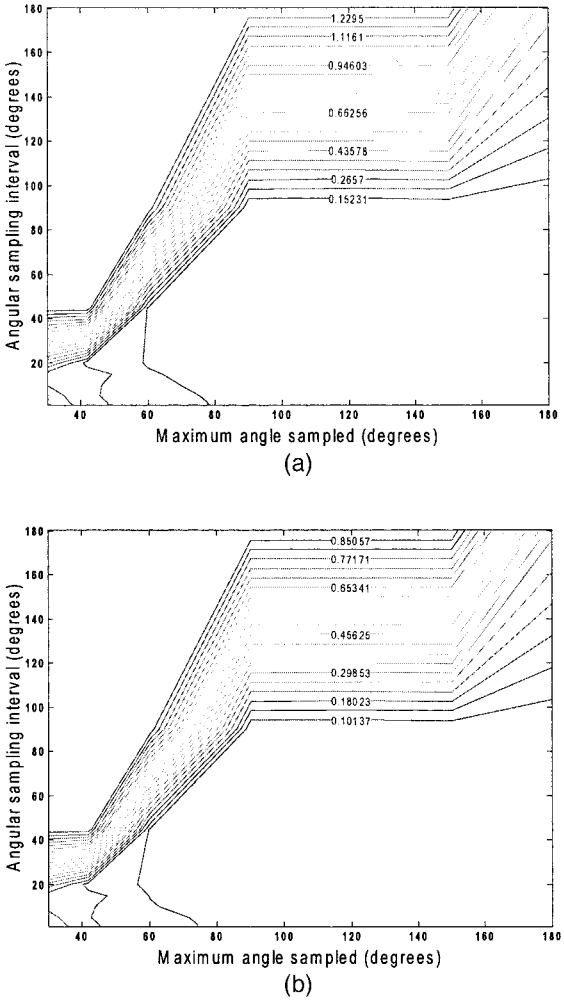

Fig. 12. Contour plots demonstrating the dependence of ε_{avg} on both $\Delta\theta$ and θ_{MAX} for a fixed optical property set of $\mu_a = 0.5\ cm^{-1}$ and $\mu_s' = 10\ cm^{-1}$ for both (a) μ_a and (b) μ_s' .

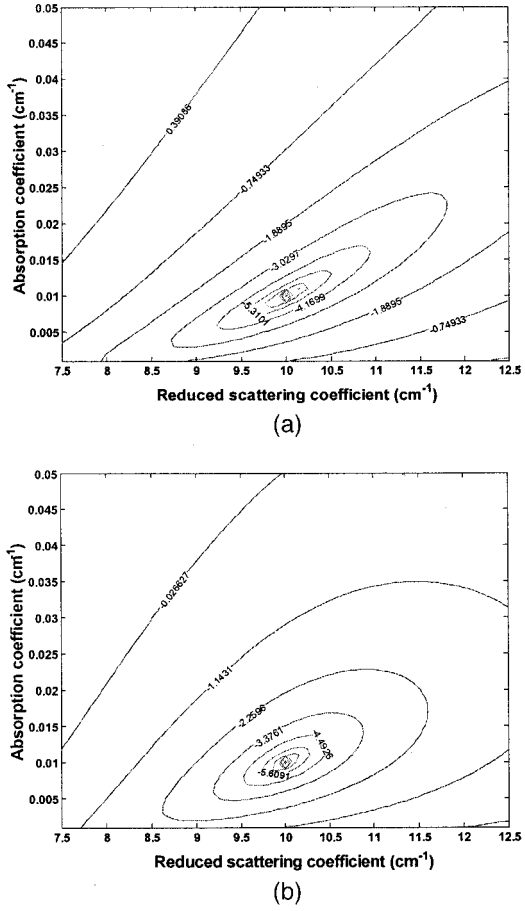

Fig. 13. χ^2 space calculated for a (a) two sensor measurements at 0.5 and 1.5 cm and (b) a single-sensor measurement at 0.5 cm by use of a μ_{eff} constraint. The true optical properties are $\mu_a = 0.01\ cm^{-1}$ and $\mu_s' = 10\ cm^{-1}$.

measurements or constraints can improve fitting performance. Consider the inverse of the slope, S, in Eq. (6):

$$\frac{1}{S} = \frac{\mu_{eff}}{r} + \frac{\mu_{eff} + 3\mu_a}{3\mu_{eff}^2}. \tag{12}$$

Examining Eq. (12), we see that the slope of $1/S$ versus $1/r$ is a function of μ_{eff}, whereas the intercept contains both μ_{eff} and μ_a.

Therefore, relative radiance measurements at multiple positions may provide improvements in optical property recovery. Experimentally, multiple radiance sensors have the advantage that they do not need to be calibrated relative to one another. Conversely, as the method is based on a change in slopes, it requires reasonable separation between sensors for unique recovery of optical properties. As shown in Figs. 4 and 5, different sensor positions result in a change in the χ^2 topography even for the same optical properties. However, for all sensor positions the global minimum intersects at the true solution. Therefore, adding the χ^2 space of different sensor positions increases the regions surrounding the true solution, thereby leading to a more pronounced global minimum. Conversely, as $r_1 \to r_2$ the terrain approaches the χ^2 topography of a single sensor.

Figure 13(a) demonstrates how the χ^2 topography converges to a more-localized minimum [compared with Fig. 4(b)] when relative radiance information at both the 0.5 and the 1.5 cm positions is fitted simultaneously. To generate Fig. 13(a) we adapted Eq. (7) by adding the χ^2 values for both sensor positions. In all cases, the $P3$ approximation was used as the forward model in the calculations.

An even more pronounced minimum is produced if μ_{eff} is utilized as a constraint during fitting. Such a strategy is easily seen from Eq. (12), for which knowledge of μ_{eff} results in a unique solution for μ_a. Figure 13(b) illustrates how the χ^2 topography results in an even more distinct global minimum when a known μ_{eff} is used during fitting. Again, we generated the resultant χ^2 plot by adapting the χ^2 function in Eq. (7) to include the χ^2 difference with the known μ_{eff}.

Finally, Fig. 14 plots ε_{avg} for μ_a and μ_s' as a function of true μ_a (0–5 cm^{-1}) and for a fixed $\mu_{s,true}'$

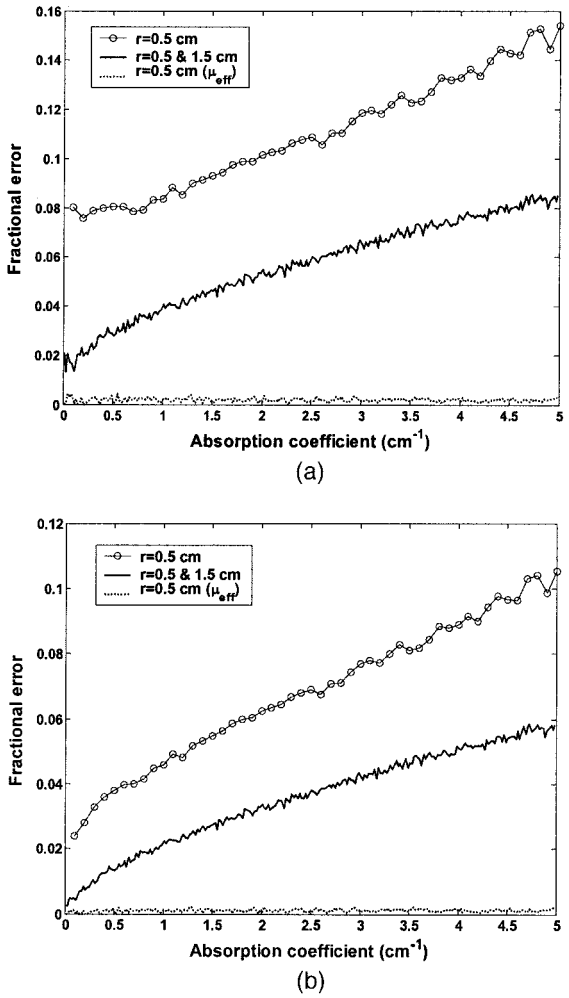

Fig. 14. Fractional uncertainty in recovered (a) μ_a and (b) μ_s' owing to noise for true optical properties of $\mu_s' = 10\ \mathrm{cm}^{-1}$ and μ_a ranging from 0.001 to 5 cm^{-1}. The cases illustrated are a single sensor with (dashed curve) and without a μ_{eff} constraint (circles), and two sensors (solid curve).

$= 10\ \mathrm{cm}^{-1}$ at $r = 1$ cm. The simultaneous fitting of two sensors at 0.5 and 1.5 cm reduces the fractional uncertainty almost twofold compared with a single-sensor fit, while the application of a μ_{eff} constraint provides virtually unique optical property recovery even in the presence of noise.

11. Discussion and Conclusions

We have performed an analysis of absolute optical property quantification by using relative steady-state radiance measurements at a single position. The analysis provides several general conclusions regarding optical property characterization with point steady-state relative radiance measurements.

Using the $P3$ approximation, we have studied the χ^2 response surface for relative radiance measurements at a single position and demonstrated that the radiance profile can be used to uniquely characterize optical properties under noiseless experimental conditions. However, under noisy conditions an expanded set of possible solutions emerges that leads to uncertainty in recovered optical properties.

By employing similarity relations for relative radiance measurements in the $P1$ approximation we have presented an analytical technique with which to study the effects of noise. Using this method, we have studied the optical property regimes in which radiance characterization is most accurate. Based on our analysis, we have shown that significant uncertainty exists in characterizing highly scattering and highly absorbing media and that radiance characterization is best performed when $\sim\mu_s' \leq 11\ \mathrm{cm}^{-1}$ and $\mu_a \leq 2\ \mathrm{cm}^{-1}$. We have further explored optimal experimental configurations for radiance optical property recovery. Our results indicate that a minimum of three relative radiance measurements sampling the 0°, 90°, and 180° detection angles at a sensor position no greater than 1 cm can be used to optimally characterize optical properties. This observation carries interesting implications for the optimal design of radiance systems. First, the vital information content for optical property recovery requires that measurements be sampled to a minimum angle of 90° or greater. In the case of radiance systems that use mechanical rotation, acquisition time can be almost halved compared with that for 0°–180° angles. However, an implication of the above analysis is that mechanical rotation may not be necessary because only two measurements are required for optimal information content. This may facilitate the packing of two small radiance sensors into a single fiber at fixed angular positions. In addition to increasing acquisition speed, such a design carries the further advantage that uncertainties are greatly reduced because of the absence of angular rotation errors.

Finally, by examining the diffusion approximation expression for radiance we have indicated two strategies for improving optical property quantification. Our results show that adding a μ_{eff} constraint to a single-sensor radiance fit greatly reduces noise sensitivity and allows for significant improvements in optical property recovery. Experimentally, the advantage of this method is that measurements at multiple points can be used to determine μ_{eff} without the necessity for absolute calibration, although the sensors must be calibrated relative to one another. Clinically, an array of optical sensors positioned at different locations in the tissue[18] may be used to assess μ_{eff}, with individual sensors used to produce an average set of optical properties. Alternatively, two radiance measurements at different spatial positions can be used to reduce noise sensitivity without the necessity for a μ_{eff} constraint. Furthermore, these sensors do not need to be calibrated relative to one another, although quantification accuracy will likely be dependent on their relative spacing.

We believe that the results of this analysis along with the previous work of Dickey *et al.*[6] indicate the potential of point radiance measurements as an alternative to traditional fluence-based methods for quantifying the optics of homogeneous turbid media.

Although radiance measurements were previously used to characterize tissue properties for photodynamic therapy, our lab has recently demonstrated the improved sensitivity of directional radiance measurements for on-line monitoring of heterogeneous scattering media during laser interstitial thermal therapy.[5,18] In conjunction with this work, we expect that in the future an array of radiance sensors may be used to characterize tissue optical properties before laser interstitial thermal therapy is performed for on-site treatment planning and subsequently to monitor on-line changes in tissue properties during laser heating to determine the extent of thermal coagulation.

Financial support for this research was provided by the National Cancer Institute of Canada (with funds from the Canadian Cancer Society) and the Natural Sciences and Engineering Research Council of Canada. The authors thank Brian Wilson, John Tulip, and Dwayne Dickey for helpful discussions and insight and Sean Davidson for editing of the manuscript.

References

1. D. R. Wyman, M. S. Patterson, and B. C. Wilson, "Similarity relations for the interaction parameters in radiation transport," Appl. Opt. **28,** 5243–5249 (1989).
2. L. Lilge, N. Pomerleau-Dalcourt, A. Douplik, S. H. Selman, R. W. Keck, M. Szkudlarek, M. Pestka, and J. Jankun, "Transperineal *in vivo* fluence-rate dosimetry in the canine prostate during SnET2-mediated PDT," Phys. Med. Biol. **49,** 3209–3225 (2004).
3. T. C. Zhu, A. Dimofte, J. C. Finlay, D. Stripp, T. Busch, J. Miles, R. Whittington, S. B. Malkowicz, Z. Tochner, E. Glatstein, and S. M. Hahn, "Optical properties of human prostate at 732 nm measured *in vivo* during motexafin lutetium-mediated photodynamic therapy," Photochem. Photobiol. **81,** 96–105 (2005).
4. O. Bajaras, A. M. Ballangrud, G. G. Miller, R. B. Moore, and J. Tulip, "Monte Carlo modeling of angular radiance in tissue phantoms and human prostate: PDT light dosimetry," Phys. Med. Biol. **42,** 1675–1687 (1997).
5. L. C. L. Chin, B. C. Wilson, W. M. Whelan, and I. A. Vitkin, "Radiance-based monitoring of the coagulation boundary during laser interstitial thermal therapy," Opt. Lett. **29,** 959–961 (2004).
6. D. J. Dickey, R. B. Moore, D. C. Rayner, and J. Tulip, "Light dosimetry using the *P*3 approximation," Phys. Med. Biol. **46,** 2359–2370 (2001).
7. L. G. Henyey and J. L. Greenstein, "Diffuse radiation in the galaxy," Astrophys. J. **93,** 70–83 (1941).
8. J. C. Finlay and T. H. Foster, "Hemoglobin oxygen saturations in phantoms and *in vivo* from measurements of steady-state diffuse reflectance at a single, short source-detector separation," Med. Phys. **31,** 1949–1959 (2004).
9. K. M. Case and P. F. Zweifel, *Linear Transport Theory* (Addison-Wesley, 1967).
10. E. L. Hull, and T. H. Foster, "Steady-state reflectance spectroscopy in the *P*3 approximation," J. Opt. Soc. Am. A **18,** 584–599 (2001).
11. D. A. Boas, "Diffuse photon probes of structural and dynamical properties of turbid media: theory and biomedical applications," Ph.D. dissertation (University of Pennylvania, 1996).
12. F. Martelli, M. Bassani, L. Alianelli, L. Zangheri, and G. Zaccanti, "Accuracy of the diffusion equation to describe photon migration through an infinite medium: numerical and experimental investigation," Phys. Med. Biol. **45,** 1359–1373 (2000).
13. J. P. Marijnissen and W. M. Star, "Calibration of isotropic light dosimetry probes based on scattering bulbs in clear media," Phys. Med. Biol. **41,** 1191–1208 (1996).
14. J. P. Marijnissen and W. M. Star, "Performance of isotropic light dosimetry probes based on scattering bulbs in turbid media," Phys. Med. Biol. **47,** 2049–2058 (2002).
15. L. H. Wang, S. L. Jacques, and L. Zheng, "MCML—Monte Carlo modeling of light transport in multilayered tissues," Comput. Methods Programs Biomed. **47,** 131–146 (1995).
16. L. Chin, M. Pop, W. Whelan, M. Sherar, and A. Vitkin, "Optical method using fluence or radiance measurements to monitor thermal therapy," Rev. Sci. Instrum. **74,** 393–395 (2003).
17. F. Bevilacqua and C. Depeursinge, "Monte Carlo study of diffuse reflectance at source–detector separations close to one transport mean free path," J. Opt. Soc. Am. A **16,** 2935–2945 (1999).
18. W. W. Whelan, P. Chun, L. C. Chin, M. D. Sherar, and I. A. Vitkin, "Laser thermal therapy: utility of interstitial fluence monitoring for locating optical sensors," Phys. Med. Biol. **46,** N91–N96 (2001).